



**HAL**  
open science

# Interferences in the re-emission field of multimodal leaky Lamb waves propagating in an immersed plate analytical modelling, simulation and experimentation

P. Kauffmann, Ma. Ploix, Jf. Chaix, C. Gueudre, G. Corneloup, F. Baque

## ► To cite this version:

P. Kauffmann, Ma. Ploix, Jf. Chaix, C. Gueudre, G. Corneloup, et al.. Interferences in the re-emission field of multimodal leaky Lamb waves propagating in an immersed plate analytical modelling, simulation and experimentation. *Journal of Sound and Vibration*, 2020, 10.1016/j.jsv.2019.115015 . cea-02339736

**HAL Id: cea-02339736**

**<https://cea.hal.science/cea-02339736>**

Submitted on 21 Dec 2021

**HAL** is a multi-disciplinary open access archive for the deposit and dissemination of scientific research documents, whether they are published or not. The documents may come from teaching and research institutions in France or abroad, or from public or private research centers.

L'archive ouverte pluridisciplinaire **HAL**, est destinée au dépôt et à la diffusion de documents scientifiques de niveau recherche, publiés ou non, émanant des établissements d'enseignement et de recherche français ou étrangers, des laboratoires publics ou privés.



Distributed under a Creative Commons Attribution - NonCommercial 4.0 International License

1 Title

2 Interferences in the re-emission field of multimodal leaky Lamb waves propagating in  
3 an immersed plate: analytical modelling, simulation and experimentation

4

5 Authors' names and affiliations

6 Pierre KAUFFMANN<sup>1,2</sup>, Marie-Aude PLOIX<sup>1,\*</sup>, Jean-François CHAIX<sup>1</sup>, Cécile  
7 GUEUDRE<sup>1</sup>, Gilles CORNELOUP<sup>1</sup>, François BAQUE<sup>2</sup>

8

9 <sup>1</sup> Aix Marseille Univ, CNRS, Centrale Marseille, LMA, Laboratoire de Mécanique et  
10 d'Acoustique, Waves and Imaging group, Aix en Provence, France

11

12 <sup>2</sup> CEA Cadarache DEN/DTN/STCP/LISM (Laboratoire d'Instrumentation, Systèmes et  
13 Méthodes), Saint Paul Lez Durance, France

14

15

16

17 \*Corresponding author

18 Phone number: +33 (0) 4 42 93 90 84

19 E-mail address: marie-aude.ploix@univ-amu.fr

20 Postal Address: Laboratoire de Mécanique et d'Acoustique, CNRS - UMR 7031

21 Aix Marseille Université, IUT GMP

22 413 Avenue Gaston Berger

23 13 625 Aix en Provence Cedex 1

24

25 **Abstract**

26 The transmission and re-emission of energy by leaky Lamb waves from an immersed  
27 plate is being studied in the case of multi-modal propagation. When more than two  
28 Lamb modes propagate together, interferences can be generated in the re-emitted field.  
29 The latter have to be well understood and mastered because they can distort the  
30 diagnosis of a Non-Destructive Testing of an immersed plate. They are experimentally  
31 observed with C-scan visualisation, but they are not consistent with the Bertoni and  
32 Tamir model which describes the theoretical re-emitted acoustic field by leaky Lamb  
33 modes excited by an incident ultrasonic beam. The same interferences are also observed  
34 by finite-element simulation. The Bertoni and Tamir model is then modified to take into  
35 account the incidence of side lobes generated by an immersed ultrasonic transducer.  
36 That way, the same interferences observed are theoretically predicted, confirming that  
37 side lobes are the cause of it. Side lobes can generate a second leaky Lamb mode which  
38 propagate and interfere with the mode generated by the main acoustic beam. This  
39 secondary Lamb mode is non-negligible if it has higher leaky attenuation than the  
40 targeted mode. Thus, to avoid multi-modal generation with an incident beam, the best  
41 method is to aim at the leaky Lamb mode with the highest leaky attenuation coefficient  
42 at the chosen frequency.

43

44 **Keywords**

45 Leaky Lamb wave; re-emission; re-emitted field; transmitted field; leaky attenuation;  
46 interferences; multi-modal propagation

47

48 **1. INTRODUCTION**

49 The sodium-cooled fast reactor (SFR) technology has been chosen for the 4<sup>th</sup>  
50 generation of nuclear power plants in France. With liquid sodium as the coolant,  
51 improvement of in-service inspection and repair (ISI&R) techniques has been identified  
52 as a major issue for the ASTRID project (Advanced Sodium Technological Reactor for  
53 Industrial Demonstration) [1,2]. Ultrasonic solutions are being studied for the inspection  
54 of the main vessel and different internal parts of ASTRID: waves guided in elastic  
55 plates (Lamb waves) seem to be suitable candidates to achieve this objective [3,4]. The  
56 final objective of this work will be then to perform NDT in several parallel and  
57 immersed plates by using Lamb waves.

58 Lamb waves are frequently used for long-range non-destructive testing (NDT) of  
59 plates [5–10]. When the structure to be controlled is immersed in a fluid, Lamb waves  
60 leak energy into the surrounding fluid, which is why they are called leaky Lamb waves  
61 [10–14]. This is the case for the ASTRID main vessel filled with liquid sodium. To  
62 understand the physical phenomena occurring in such conditions, we decided to study  
63 the similar case of a stainless steel plate in water (given the wide diameter of the vessel,  
64 about 15 meters, we primarily choose to approximate it locally as a plate). In the case of  
65 a steel plate immersed in water, it has been shown that variations induced by the  
66 surrounding fluid on Lamb wave velocities are negligible [15]. However, leaky Lamb  
67 waves are highly attenuated, and this reduces the inspection range. To overcome this  
68 issue, we can use leaky Lamb modes with dominant longitudinal displacements and  
69 therefore with almost no leaky damping [16,17]. However, by reciprocity, these modes  
70 are particularly difficult to excite using a bounded-beam incident at a Lamb-wave  
71 generating angle [16].

72 The oblique incidence technique is widely used to generate leaky Lamb waves in an  
73 immersed plate: the required leaky Lamb mode is selected by the incidence of an  
74 acoustic beam generated by an immersed transducer or through a wedge  
75 [4,5,7,10,13,18–21]. This technique may result in the excitation of several leaky Lamb  
76 modes together because of the beam-spreading angle, thereby opening the door to multi-  
77 modal propagation [5].

78 In the case of multi-modal propagation, we can observe spatial interferences in the  
79 acoustic field emitted by the plate in the fluid [22–24]. Moreover, as a function of the  
80 defect, the creation of others Lamb modes can occur when the incident Lamb mode is  
81 reflecting on the defect. Thus, it can also lead to multi-modal propagation. The  
82 interferences in the re-emitted field could eventually complicate the diagnosis of NDT,  
83 and then they have to be well understood.

84 To compute the acoustic field reflected by and transmitted through a plate, an  
85 analytical model has been developed in reference [18], applied to the case of leaky  
86 Lamb waves in references [25,26], and numerically solved to take into account multi-  
87 modal propagation generated by the main incident beam in references [27,28]. This  
88 analytical model is referred to as the Bertoni and Tamir model in this paper. This model  
89 had never been used to study multi-modal interferences until now. The Bertoni and  
90 Tamir model takes into account the angle spreading of the acoustic beam, but it does not  
91 take into account the effect of side lobes inevitably generated by a real transducer. This  
92 effect has not been studied for the case of leaky Lamb waves, except in the recently  
93 published reference [29] which discusses finite-element simulations (FEM) of a  
94 complete acoustic field incident on a plate, but only for the normal incidence. We will  
95 show that side lobes can generate different leaky Lamb modes to that targeted by the

96 main beam under specific conditions, and we adapted the Bertoni and Tamir model in  
97 order to completely model all these phenomena.

98 In the first section, we present the general background of generation and re-emission  
99 of leaky Lamb waves, as well as the initial Bertoni and Tamir model. We  
100 experimentally highlight the presence of interferences in the re-emitted acoustic field in  
101 a configuration where the Bertoni and Tamir model does not predict any. Then, the  
102 Bertoni and Tamir model is modified to take into account the effect of side lobes on  
103 leaky Lamb mode generation. This clarifies the generation of leaky Lamb modes that  
104 lead to multi-modal propagation.

105

## 106 **2. GENERATION AND RE-EMISSION: THEORETICAL AND EXPERIMENTAL**

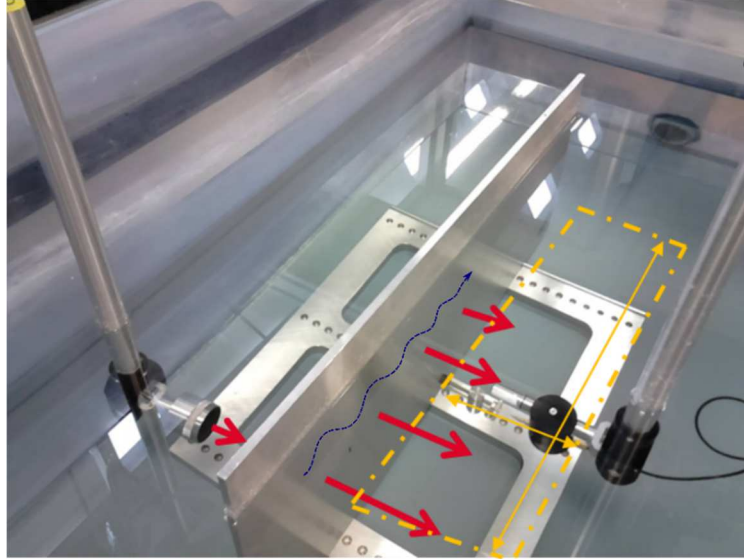
### 107 **BACKGROUND**

#### 108 **2.1. Generalities on generation, leakage and interferences**

109 Lamb waves are generated in immersion with oblique incidence technique. For the  
110 sake of clarity, the same configuration is used in this paper and hereafter referred to as  
111 "our configuration": it refers to one stainless steel plate 7.8 mm thick, with an acoustic  
112 beam incident at an angle  $\theta$  (different incidences will be tested), generated by a 500  
113 kHz central frequency transducer (i.e. a product frequency x thickness of 3.9 MHz.mm)  
114 with an active diameter of 38.1 mm. Other numerical values that were used as input in  
115 the modelling are given in the appendix.

116 In order to visualize the experimental re-emitted field, Cscan acquisitions are  
117 performed and results are presented all along the paper. A picture of the experimental  
118 bench is shown in Figure 1. The transducer sends a wave train of 40 cycles at 500 kHz  
119 at the chosen incident angle  $\theta$ . We choose a long wave train (40 cycles of sinusoid)  
120 because it is long enough to approximate the steady state. The transmitted field is

121 scanned and recorded by a needle hydrophone ( $\varnothing$  0.5 mm) in the area perpendicular to  
122 the plate shown in dashed-dotted lines.

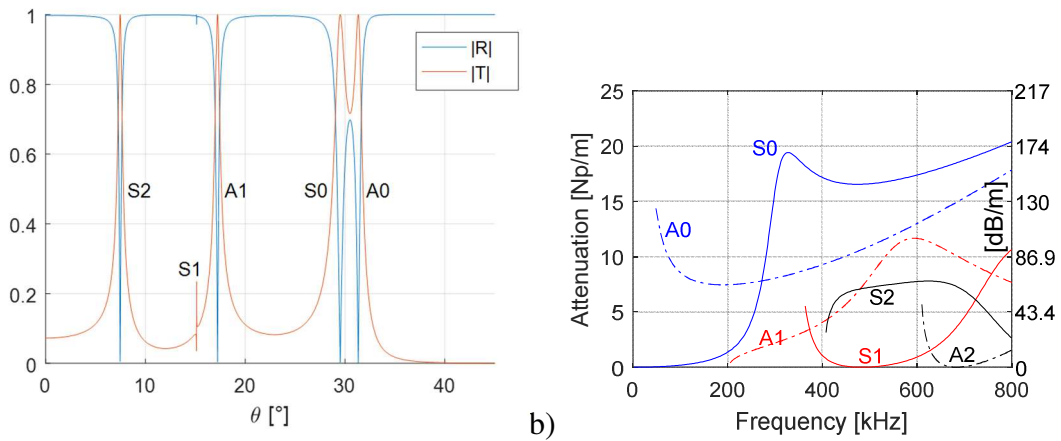


123  
124 Figure 1: Experimental bench: incident bulk waves are sent by a transducer onto a plate  
125 immersed in water (7.8 mm thick and 700 mm long). Leaky Lamb waves are generated  
126 (symbolized by dashed blue arrow), and the transmitted acoustic field (bold red arrows) is  
127 scanned by a needle hydrophone in an area perpendicular to the plate (dash-dotted yellow line).

128  
129 The plane wave reflection and transmission coefficients of the immersed plate are  
130 plotted as a function of the incident angle  $\theta$  in Figure 2.a. These coefficients were  
131 calculated on the basis of reference [27] and will be applied later in the Bertoni and  
132 Tamir model. They provide a convenient way of visualising angles generating leaky  
133 Lamb modes that are characterised by a complete transmission and null reflection. Thus,  
134 in our configuration, S2 is generated at  $\theta = 7.6^\circ$ , S1 at  $\theta = 15^\circ$ , A1 at  $\theta = 17.2^\circ$ , S0 at  
135  $\theta = 29.5^\circ$  and A0 at  $\theta = 31.3^\circ$ .

136 Besides the leaky attenuation coefficient that quantifies leakage into the fluid [16]  
137 was calculated for each mode and is represented in Figure 2.b. It was calculated on the

138 basis of the formulation published in reference [12]. Its knowledge allows to provide for  
 139 the level of re-emission of a mode, and by reciprocity the ability to generate a mode in  
 140 the plate. For example, at 300 kHz, S0 presents the maximum of leaky attenuation  
 141 coefficient and then will be the best mode available to be generated with oblique  
 142 incidence technique. At the same time, it will be quickly attenuated along the plate and  
 143 then will not be able to test long distance.



144 a) Theoretical reflection and transmission modulus at 500 kHz of the immersed  
 145 stainless-steel plate as a function of the incidence angle  $\theta$ . b) Theoretical leaky attenuation  
 146 coefficient of Lamb modes for a stainless-steel plate with a thickness of 7.8 mm.  
 147

148  
 149 When a single mode is generated, the leakage along the plate is directed with the  
 150 same angle as incident one [10-12]. When several modes are generated simultaneously  
 151 in the immersed plate, their different leakages (with different directions) interfere with a  
 152 constructive or destructive manner and can result in a new apparent leakage direction.  
 153 The theoretical direction of these interference fringes for two different leaky Lamb  
 154 modes (with directions  $\theta_1$  and  $\theta_2$ ) is given by equation 1 from references [23,24]:

$$\theta_s = -\arctan\left(\frac{\cos(\theta_2) - \cos(\theta_1)}{\sin(\theta_2) - \sin(\theta_1)}\right) \quad (1)$$



155 where  $\theta_s$  is the direction of interferences,  $\theta_1$  and  $\theta_2$  the respective re-emission direction  
 156 of leaky Lamb modes 1 and 2 that are propagating together.

157

## 158 **2.2. The Bertoni and Tamir model**

159 This part outlines the initial Bertoni and Tamir model. The model is then applied and  
 160 compared to experimentation, and their limitations in our configuration are shown.

### 161 **2.2.1. Principle**

162 The Bertoni and Tamir model is an analytical model solved numerically to compute  
 163 the reflected and transmitted steady state acoustical fields by an immersed plate. This  
 164 model is extensively described in [27] and the same notations will be used, except for  
 165 the half-width of the incident beam and its projection onto the plate that are noted  $r$  and  
 166  $r_0$  respectively (instead of  $w$  and  $w_0$ ) and the half-width spreading angle of the incident  
 167 beam that is noted  $\Theta_{HW}$  (instead of  $W_v$ ).

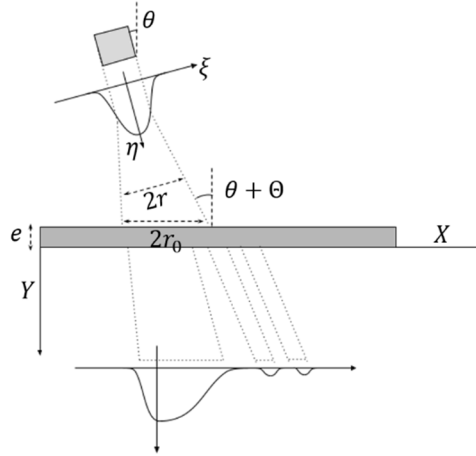
168 The plate is considered made of a homogeneous linear elastic isotropic medium.  
 169 Coordinate systems are shown in Figure 3. The  $X$  and  $Y$  axes are associated with the  
 170 plate (with  $X$  being parallel to the surface of the plate) and the  $\xi$  and  $\eta$  axis are linked  
 171 with the incident acoustic beam (with  $\xi$  perpendicular to the incident acoustic beam).  
 172 The incidence of the beam is centred on the angle  $\theta$ , with a half-width spreading angle  
 173  $\Theta$  (for which two definitions will be used, noted  $\Theta_{HW}$  and  $\Theta_0$ , see below).

174 The Bertoni and Tamir model defines the incident acoustic field as a superposition of  
 175 an infinite number of plane waves having the same wavelength but different incidence  
 176 angles, through the following Fourier integral transforms [27]:

$$U_{inc}(X, Y) = \frac{1}{2\pi} \int_{k-\pi/r_0}^{k+\pi/r_0} V(k_X) \exp[i(Xk_X + Yk_Y)] dk_X \quad (2)$$

$$\text{and } V(k_X) = \int_{-r_0}^{r_0} U_{inc}(X, -e) \exp(-iXk_X) dX \quad (3)$$

177 with  $k = 2\pi f/c$  the wave number in the liquid,  $c$  representing the speed of sound in the  
 178 relevant liquid,  $f$  the frequency,  $k_x$  and  $k_y$  the components of  $k$  on the  $X$  and  $Y$  axes,  
 179 and  $U_{inc}(X, -e)$  the incident amplitude at the upper surface of the plate.



180

181 Figure 3: An example of a transmitted beam profile with representation of the main acoustic  
 182 beam spreading phenomena

183

184 The propagation through the plate is then modelled by applying the plane wave  
 185 reflection or transmission coefficients (please see [27] for detailed equations). We focus  
 186 here on the way the incident beam is modelled. The incident beam is considered by the  
 187 authors to have a gaussian distribution, with an angular spreading  $\Theta$ . The definition and  
 188 quantification of  $\Theta$  may vary in the literature. We use two definitions:

189 ▪  $\Theta_{HW}$  which is defines in reference [27] as:

$$\Theta_{HW} = \sin^{-1}\left(\sin \theta + 0.53 c \cos \frac{\theta}{Df}\right) - \sin^{-1}\left(\sin \theta - 0.53 c \cos \frac{\theta}{Df}\right) \quad (4)$$

190 ▪ and  $\Theta_0$  as defined in equation (5) that gives the direction of the first zero amplitude  
 191 enclosing the theoretical main beam [30,31]:

$$\Theta_0 = \sin^{-1}\left(1.22 \frac{c}{Df}\right) \quad (5)$$

192 with and  $D$  the diameter of the emitter.

193

194 The analytical expression of Gaussian beam incident at the upper surface of the plate  
 195 ( $Y = -e$ ) used in [27] is described in equation (6):

$$U_{inc}(X, -e) = \exp \left[ -\left(\frac{X}{r_0}\right)^2 + iX \cdot k \cdot \sin(\theta) \right] \quad (6)$$

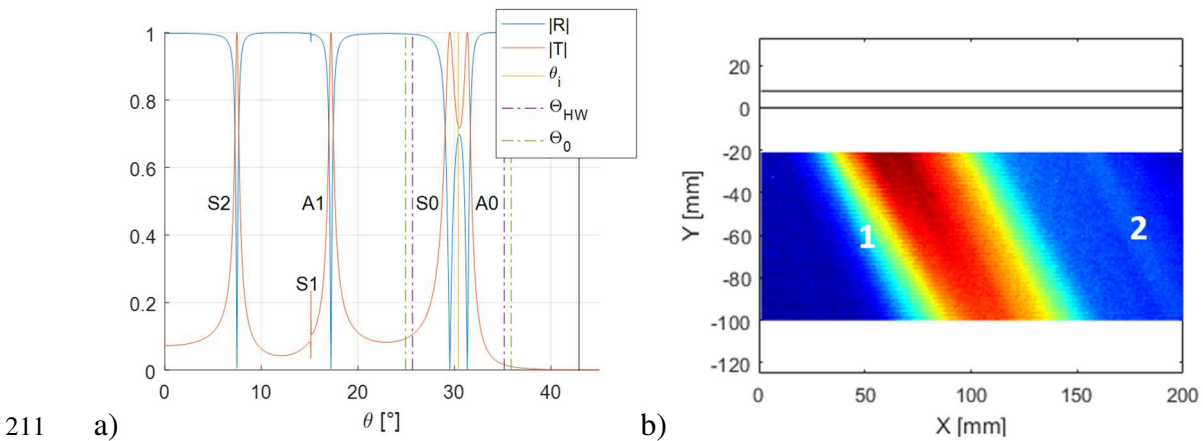
196 with  $r_0 = r/\cos(\theta)$  the projection of the beam half-width on the plate as illustrated in  
 197 Figure 3.

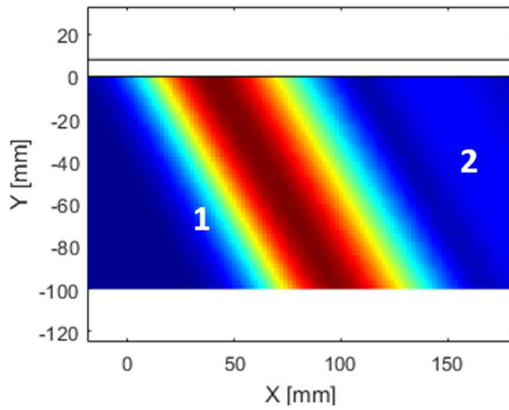
198 The equation (6) is then used as input: a spectral decomposition is applied, and the  
 199 reflected or transmitted acoustic field is integrated using the plane wave reflection and  
 200 transmission coefficients of the immersed plate that are presented in the Figure 2.a.

201

### 202 **2.2.2. Comparison to experimental measurements**

203 Experimentation with our configuration defined earlier, was performed with  $30.4^\circ$   
 204 incidence in order to generate both A0 and S0 by the main beam, as shown in Figure  
 205 4.a. One can observed one weak interference in the two acoustic fields presented,  
 206 labelled 2 in the experimentation of Figure 4.b and in Bertoni and Tamir modelling in  
 207 Figure 4.c: it is oriented at  $30^\circ$ , which is compatible with an interference between A0  
 208 and S0 according to equation (1). The experimentation is in good agreement with the  
 209 Bertoni and Tamir model. Moreover, these results show that the Bertoni and Tamir  
 210 model is able to predict interferences in the case of multimodal propagation.





212 c)

213 Figure 4: a) Reflection and transmission modulus with superposition of the main beam  
 214 spreading angles  $\Theta_{HW}$  and  $\Theta_0$  and incidence angles of side lobes for  $\theta = 30.4^\circ$  at 500kHz.  
 215 Comparison of the transmitted field: b) experimental C-scan, and c) Bertoni and Tamir model.  
 216 The plate is illustrated by two parallel black lines and is immersed on both sides.

217

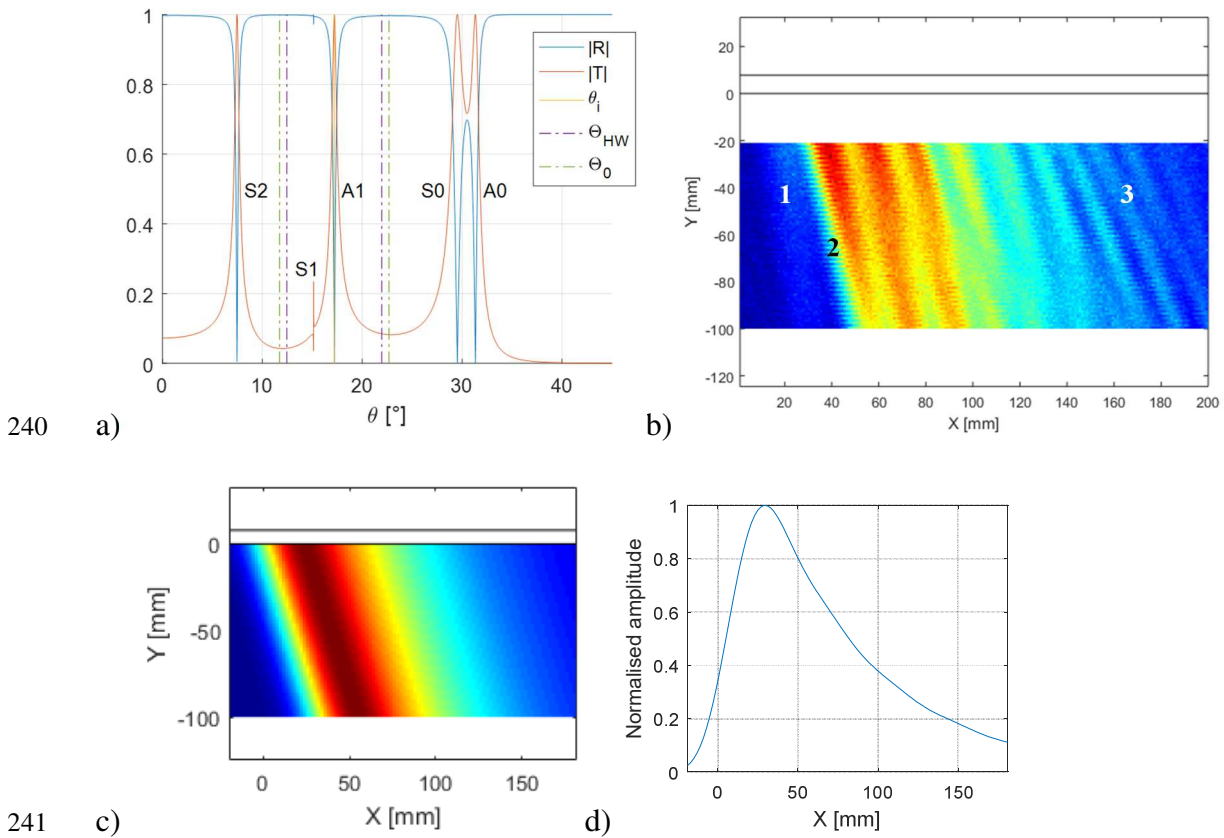
### 218 2.3. Limits of the model

219 Our configuration, this time with the incidence  $\theta = 17.2^\circ$ , implies the excitation of  
 220 two Lamb modes by the main beam: A1 and S1 (see Figure 5.a). However, S1 presents  
 221 zero re-emission at the working frequency of 500 kHz: its longitudinal displacements  
 222 are predominant, inducing almost no leakage in the fluid [16,17]. This effect is  
 223 highlighted by the null leaky attenuation coefficient of Figure 1.b. The zero attenuation  
 224 of S1 at 500 kHz is clearly visible: this mode will almost induce no re-emission and by  
 225 reciprocity will be hard to generate using an incident beam [16]. Therefore, the S1 mode  
 226 will not have any influence in this case. Thus, only A1 should be generated considering  
 227 only the main beam.

228 The C-scan image acquired in this case and represented in Figure 5.b reveals a  
 229 stripped re-emitted acoustic field. At the very beginning of the acoustic field, a weak  
 230 beam (labelled 1) is re-emitted around  $9^\circ$ . The main re-emission (labelled 2) is directed  
 231 at around  $18^\circ$ , which is compatible with the re-emission of the A1 mode excited by the

232 main beam. However, the re-emission of strips soon occurs, directed between 23° and  
 233 25° (labelled 3).

234 Figure 5.c shows the transmitted field calculated by the initial Bertoni and Tamir  
 235 model. We can observe the re-emission of the A1 mode which re-emits around 17°. The  
 236 computed acoustic field is characteristic of the re-emission of a single leaky Lamb  
 237 mode: one acoustic beam directed at a precise single angle, with an exponential  
 238 decrease in the amplitude with propagation along the plate (example of Figure 5.d). It  
 239 confirms that the contribution of the S1 mode has no measurable effect as expected.



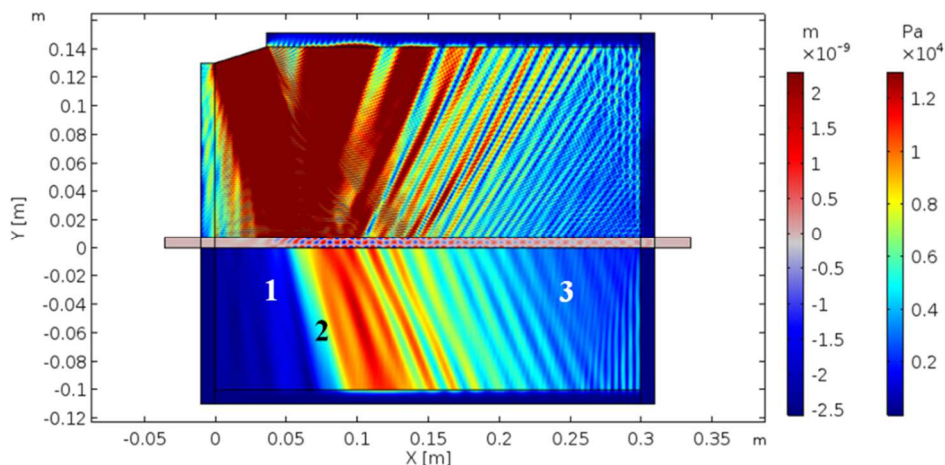
242 Figure 5: a) Reflection and transmission modulus with superposition of the main beam  
 243 spreading angles  $\Theta_{HW}$  and  $\Theta_0$  and incidence angles of side lobes for  $\theta = 17.2^\circ$  at 500kHz.  
 244 Comparison of the transmitted field: b) experimental C-scan, and c) Bertoni and Tamir model,  
 245 with d) extracted normalised amplitude for  $Y = -20$  mm.

246

247 However, the experimental and theoretical re-emitted acoustic fields are very  
248 different. This example highlights the necessity of taking into account the effect of side  
249 lobes in the modelling.

250 To ensure that experimentation is valid, we choose to confront it with finite elements  
251 simulation using the commercially available software COMSOL Multiphysics®.  
252 Calculations are made in the frequency domain to ensure the validity of the steady state  
253 hypothesis, which was made in the Bertoni and Tamir model. Since Lamb modes are  
254 purely 2D symmetrical, we use a 2D model to simplify and speed up our calculations.  
255 The transducer is classically modelled as a perfect piston source (with imposed pressure  
256 at its surface), which then generates a main beam and side lobes. Their characteristics  
257 were checked (near field length, and directions and amplitudes of the lobes) to match  
258 with our configuration.

259 Resulting reflected and transmitted field are represented in Figure 6. Perfectly  
260 matched layers (PML) were used to minimise reflections on the edges of the model.  
261 Some weak reflections still occur (because incidence angles on them are in the limits of  
262 their abilities) but they do not affect the part of interest.



263  
264 Figure 6: Transmitted acoustic field in our configuration computed with the FEM: the absolute  
265 pressure is plotted in water and vertical displacements in the plate

266

267 We can observe the same directions and interferences as in experimentation in the  
268 transmitted field: the first direction (labelled 1) at a low amplitude at  $9^\circ$ , the main beam  
269 (labelled 2) at  $17.5^\circ$ , and strips (labelled 3) oriented between  $24^\circ$  and  $25^\circ$ . This confirms  
270 the experimentation results plotted in Figure 5.b, which lead to the conclusion that the  
271 Bertoni and Tamir model is not relevant for this configuration. Since side lobes are  
272 neglected in this model, we now modify the model to take them into account.

273

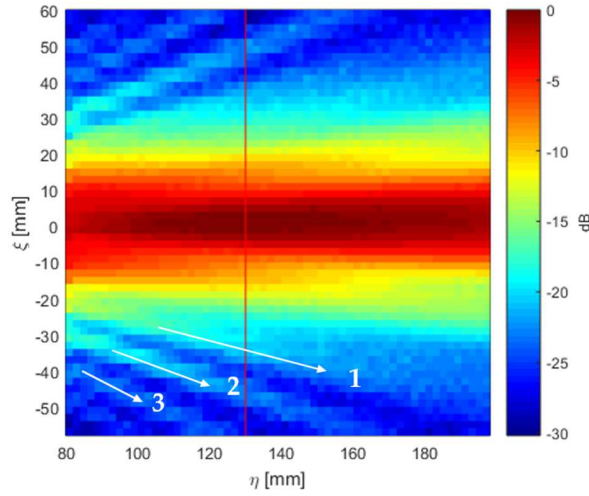
### 274 **3. MODIFICATION OF THE BERTONI AND TAMIR MODEL**

275 This part describes how side lobes were integrated in the Bertoni and Tamir model  
276 and discuss several results compared to experimentations.

#### 277 **3.1. Measurement of the experimental incident acoustic field**

278 For an accurate modelling of side lobes, we have chosen to measure the incident  
279 acoustic field emitted by the transducer (500 kHz,  $\varnothing$  38.1 mm). It is scanned with a  
280 needle hydrophone ( $\varnothing$  0.5mm). The signal is a wave train of 40 cycles at 500 kHz (the  
281 same signal used for leaky Lamb wave experimentation). The resulting C-scan is shown  
282 in Figure 7, where the red line represents the mean abscissa of the plate during  
283 experimentation. The amplitudes measured on this line are plotted further in Figure 8.

284 Side lobes can be observed at -20 dB. The directions of the side lobes in Figure 7 are  
285  $12.5^\circ$ ,  $20^\circ$  and  $26.5^\circ$  for the first, second and third side lobe respectively. We then  
286 model the amplitude and direction of these side lobes to take them into account in the  
287 Bertoni and Tamir model.



288

289 Figure 7: Experimental characterisation of the incident acoustic beam used in our configuration.

290 The red line shows the near field length, representing also the mean abscissa where the plate is  
 291 located during experimentation

292

### 293 3.2. Modeling of side lobes amplitude

294 Figure 8 shows that the Gaussian function used in Bertoni and Tamir model works  
 295 well for the main beam but does not take into account the side lobes. To take them into  
 296 account, we assessed two functions: the Bessel function of the first kind (its cardinal  
 297 form is the theoretical cross section of an acoustic beam) in equation (7), and the  
 298 Lorentz function in equation (8). Both of them were optimised with respect to the  
 299 experimental data shown in Figure 8 using a least-squares method to approach the  
 300 experimental conditions at best.

$$|U_{inc}(X, -e)| = \left| 2 \frac{J_1\left(\frac{\xi}{\beta}\right)}{\frac{\xi}{\beta}} \right| \quad (7)$$

301 with  $J_1$  representing the Bessel function of the first kind, and  $\beta$  the parameter for  
 302 optimisation which depends on the transducer, the frequency and the distance to the  
 303 transducer. For our configuration, we have  $\beta = 5.6$  mm.

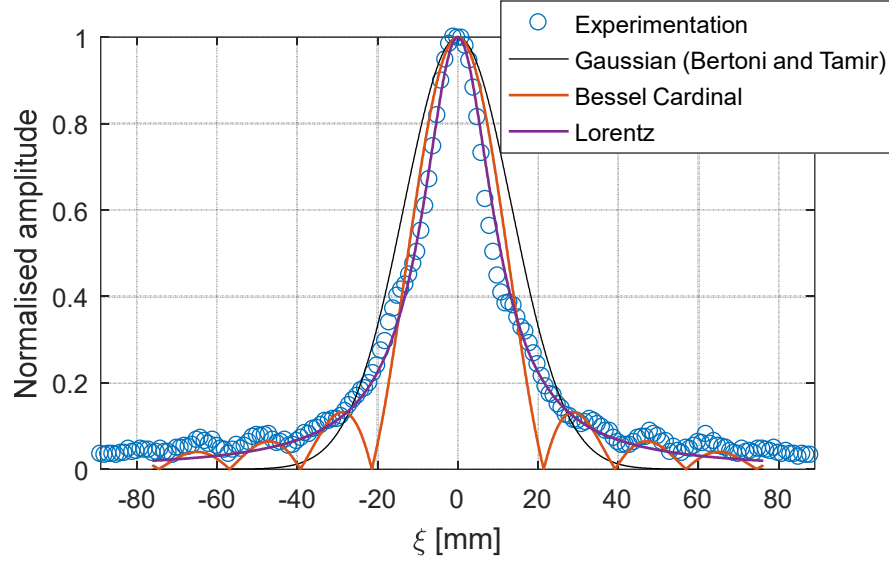


$$|U_{inc}(X, -e)| = \frac{1}{1 + \left(\frac{\xi}{\gamma}\right)^2} \quad (8)$$

304 with  $\gamma$  representing the parameter for optimisation which depends on the transducer, the

305 frequency and the distance to the transducer. For our configuration,  $\gamma = 10.8$  mm.

306



307

308 Figure 8: Incident acoustic beam profile with superposition of different model: the Bertoni and  
 309 Tamir modelling (Gaussian) and optimised least-squares models (Bessel Cardinal and Lorentz  
 310 functions)

311

312 The Bessel Cardinal function is able to well locate the side lobes and will be used to  
 313 define angles (see next paragraph). However, it introduces zero values that are not  
 314 experimentally measured. The Lorentz function appears to model the main beam and  
 315 the mean amplitude of each side lobe quite well, which is why we chose it.

316 We have integrated the amplitude of side lobes using the Lorentz function into the  
 317 modulus of  $U_{inc}(X, -e)$  in the equation (9) below.

318

319 **3.3. Modeling of side lobes directions**

320 The incidence angle of the experimentally observed side lobes has to be taken into  
 321 account into the phase of  $U_{inc}(X, -e)$ . To do so, we introduced a piecewise-defined  
 322 function  $\theta_n$  which returns the direction experimentally measured of the considered lobes  
 323 as a function of the position in the  $\xi$  axis. The correspondence with the  $X$  axis was then  
 324 easily obtained by a projection on the surface of the plate. The considered lobe itself  
 325 was identified thanks to the zeros of the Bessel function. The first four zeros used are  
 326 recalled in Table 1, with the corresponding angles experimentally measured and applied  
 327 to the case of an incidence centred on  $\theta$ .  $\beta_0 = \beta/\cos(\theta)$  is used to take into account the  
 328 projection on the surface of the plate illustrated in Figure 3.

$X/\beta_0$	$\theta_n(\frac{X}{\beta_0})$ [°]
$ X/\beta_0  < 3.83$	$\theta$
$3.83 \leq X/\beta_0 < 7.02$	$\theta + 12.5^\circ$
$7.02 \leq X/\beta_0 < 10.17$	$\theta + 20^\circ$
$10.17 \leq X/\beta_0 < 13.32$	$\theta + 26.5^\circ$

329 Table 1: Piecewise definition of  $\theta_n$  for  $X$  positive. The definition of  $\theta_n$  for  $X$  negative is based  
 330 on the same scheme, with directions symmetrical to  $\theta$

331

332 The complete formulation of the incident acoustic field is presented in equation (9):

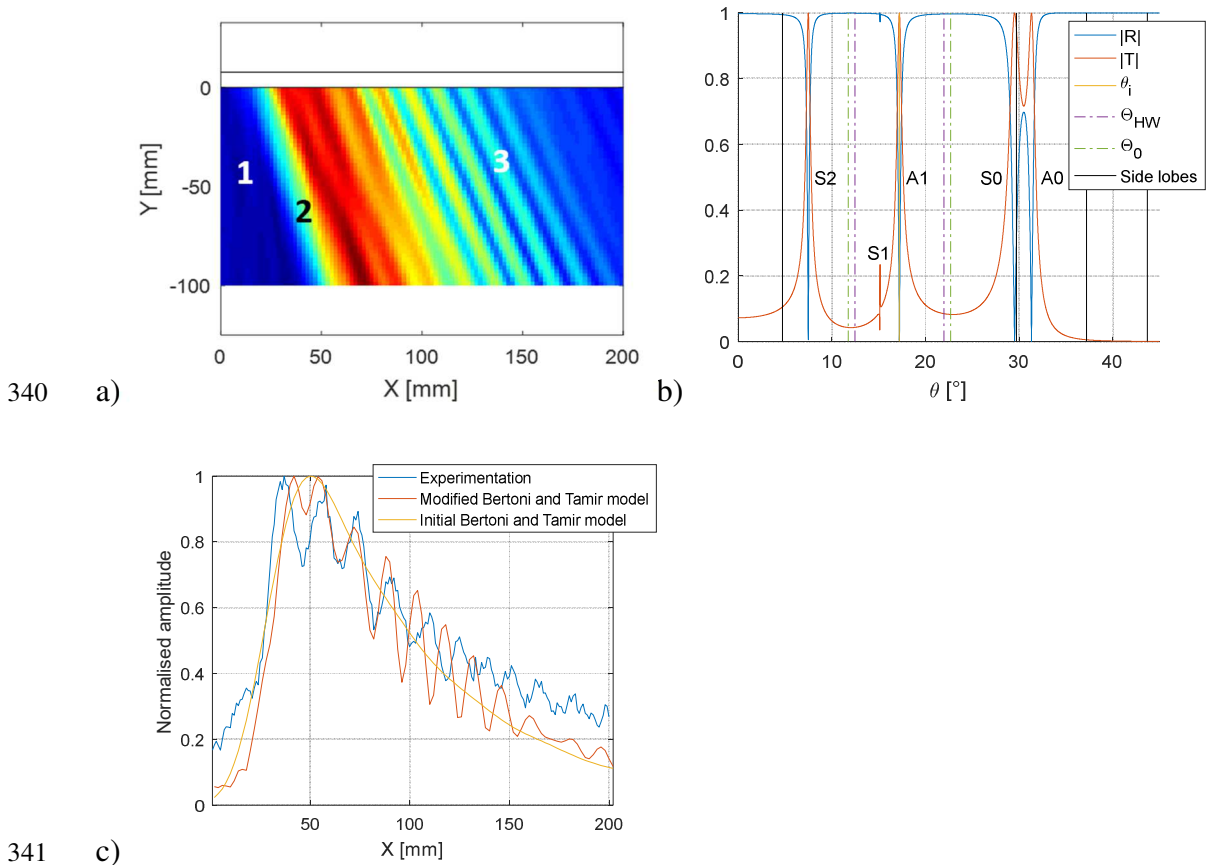
$$U_{inc}(X, -e) = \frac{1}{1 + \left(\frac{X}{\gamma_0}\right)^2} \cdot \exp \left[ i \cdot X \cdot k \cdot \sin \left( \theta_n \left( \frac{X}{\beta_0} \right) \right) \right] \quad (9)$$

333 with  $\gamma_0 = \gamma/\cos(\theta)$  and  $\beta_0$  representing optimised parameters which depend on the  
 334 transducer, the frequency and the distance to the transducer to the plate.

335 **3.4. Results and discussion**

336 **3.4.1. At 500 kHz**

337 The equation (9) was then used as input in the Bertoni and Tamir model. Numerical  
 338 values used as input in the model are given in the appendix. The new results for the case  
 339 of Figure 5 are given in Figure 9.



342 Figure 9: a) Transmitted acoustic field in our configuration computed with the modified Bertoni  
 343 and Tamir model. b) Reflection and transmission modulus with superposition of the main beam  
 344 spreading angles  $\Theta_{HW}$  and  $\Theta_0$  and incidence angles of side lobes. c) Comparison of the  
 345 amplitude at  $Y = -20$  mm for the experimentation and the Bertoni and Tamir model with and  
 346 without side lobes implementation.

347

348 The theoretical acoustic field in Figure 9.a reveals the same interferences than those  
349 observed experimentally and by FEM. At the very beginning of the acoustic field, a  
350 weak beam (labelled 1) is re-emitted around  $9^\circ$ , compatible with the re-emission of the  
351 S2 mode excited by the side lobe located left to the main beam (see incidences of side  
352 lobes in Figure 9.b). The main re-emission (labelled 2) was directed at around  $17.5^\circ$ ,  
353 which is compatible with the A1 mode excited by the main beam. The side lobe on the  
354 right of the main beam excites A0 and/or S0 modes around  $30^\circ$  (theoretically  $29.5^\circ$  for  
355 S0 and  $31.3^\circ$  for A0). These modes propagate with A1 and these three modes are  
356 reemitting together, which creates interferences. These interferences are oriented  
357 between  $24^\circ$  and  $25^\circ$  (labelled 3).

358 Moreover, the theoretical direction of these interference fringes for two different  
359 leaky Lamb modes given by equation (1) results in  $\theta_s = 23.4^\circ$  if considering S0 (with  
360  $\theta_1 = 17.2^\circ$  and  $\theta_2 = 29.5^\circ$ ) and  $\theta_s = 24.3^\circ$  if considering A0 (with  $\theta_1 = 17.2^\circ$  and  
361  $\theta_2 = 31.3^\circ$ ), which is in very good agreement with experimentation, FEM and modified  
362 Bertoni and Tamir model.

363 S0 and/or A0 modes are excited with a weaker amplitude (-20 dB) in comparison to  
364 the excitation of A1, but their leaky attenuation coefficients are greater than A1 at 500  
365 kHz (see Figure 2.b). This means that A0 and S0 are easier to excite with an incident  
366 beam and have a stronger re-emission than A1. This effect balances out the amplitude  
367 re-emitted by each mode and allows for non-negligible interferences.

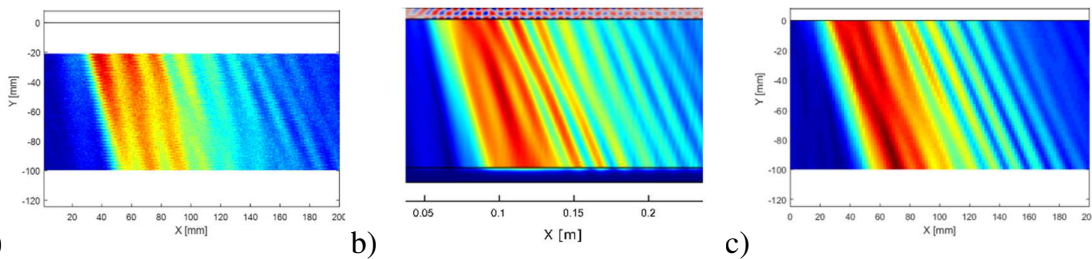
368 The improvement of the model is highlighted by the extracted amplitudes at  $Y =$   
369  $-20$  mm plotted in Figure 9.c. We can also note that a slight gap between the modified  
370 model and the experimental results tends to increase with the distance  $X$ . It can be partly  
371 explained by the fact that between labels 2 and 3, the interferences are not always

372 straight and probably indicate that more than two different Lamb modes are propagating  
373 together (probably A1, S2 and A0 and/or S0 in our configuration).

374 This proves that side lobes are indeed exciting A0 and/or S0 modes in the plate,  
375 inducing interference patterns in their re-emitted field in the fluid. This also underlines  
376 that side lobes cannot be neglected when incident at a highly attenuated Lamb mode and  
377 validates the way that the side lobes have been modelled. This point is confirmed by the  
378 other experimentations presented below.

379 Finally, the three different techniques used to study the transmitted field are brought  
380 together in Figure 10 and rescaled to simplify comparison. It can be seen that the  
381 directions and places of interference are in very good agreement between  
382 experimentation, FEM and the modified analytical model.

383



384

a)

b)

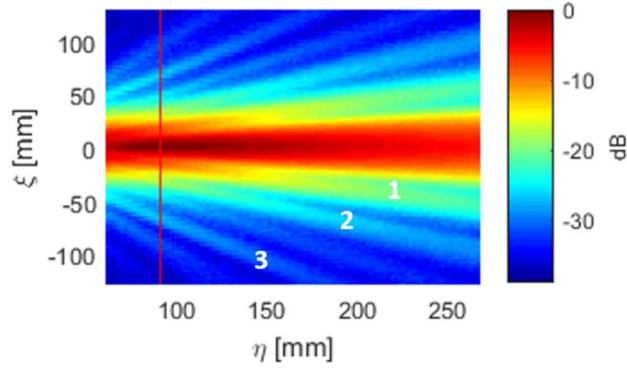
c)

385 Figure 10: Comparison of the transmitted field on the same scale: a) experimental C-scan, b)  
386 finite-element simulation and c) modified analytical Bertoni and Tamir model

387

### 388 **3.4.2. At 250 kHz**

389 Other experimentations have been performed at 250 kHz with another transducer ( $\emptyset$   
390 46 mm, central frequency at 250 kHz) and compared to the results of the modified  
391 model. The new incident acoustic field has been characterised in Figure 11 with the  
392 same protocol as previously.



393

394 Figure 11: Experimental characterisation of the incident acoustic beam used at 250 kHz. The red  
 395 line shows the near field length, representing the mean abscissa where the plate is located during  
 396 experimentation

397

398 This leads to new values of the  $\beta$  and  $\gamma$  in equations (7) and (8): respectively 5.5 mm  
 399 and 12.5 mm. The incidence of the first three lobes labelled in Figure 11 have been  
 400 measured at  $11.5^\circ$ ,  $21^\circ$  and  $28^\circ$ . These new parameters have been used as input of our  
 401 modified Bertoni and Tamir model to take into account the incidence of side lobes.

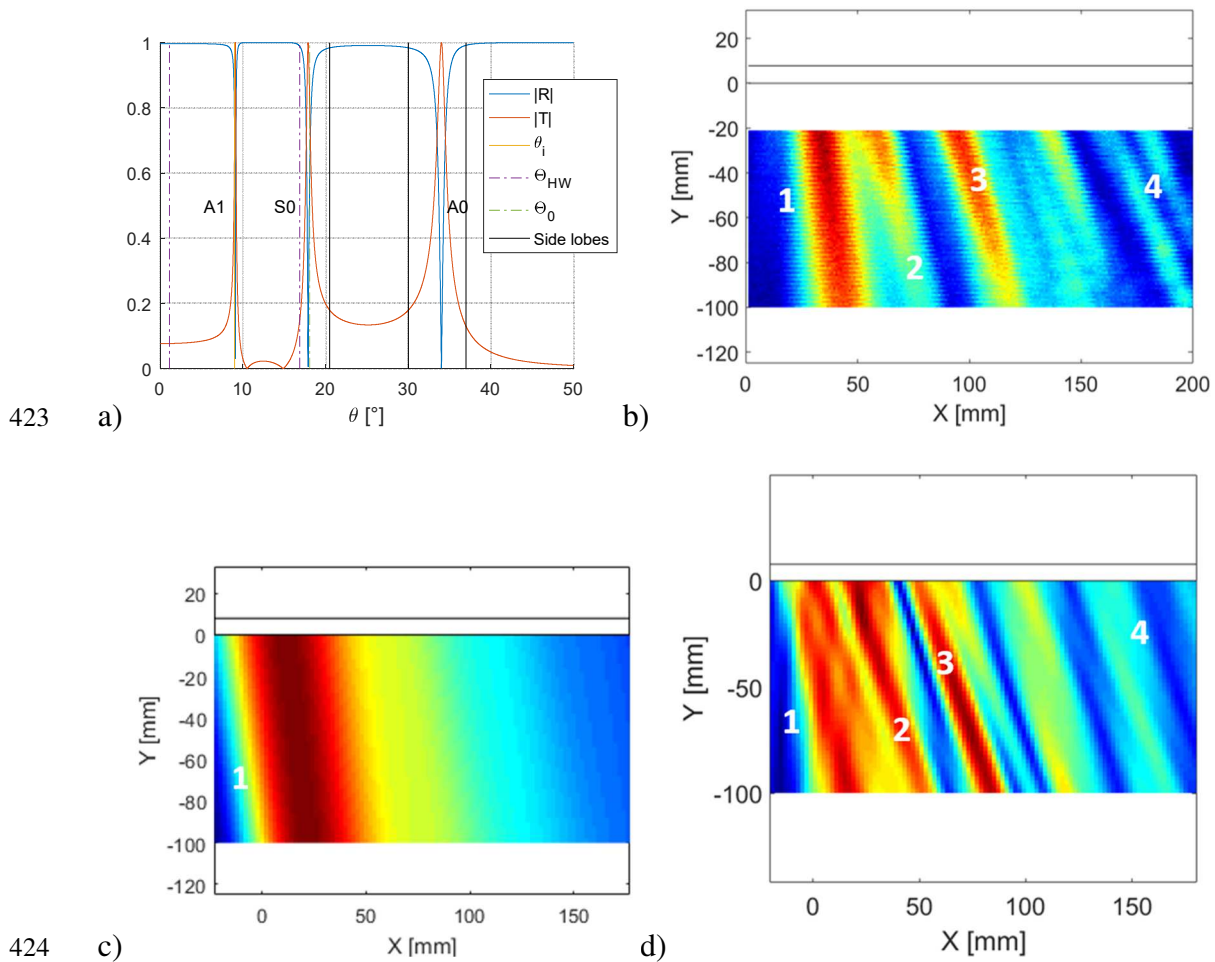
402 Two different incidence angles are applied successively with this transducer:  $\theta = 9^\circ$   
 403 to generate the A1 mode (Figure 12) and  $\theta = 34.2^\circ$  to generate A0 (Figure 13).

404 The A1 mode (at  $\theta = 9^\circ$ ) is the mode with the smallest leaky attenuation at 250 kHz  
 405 (see Figure 2.b), which means that A0 and S0 modes will be easier to generate. The  
 406 Figure 12.a shows that the S0 mode at  $18.2^\circ$  is at the extreme incidence of the main  
 407 beam to be excited by it. However, this mode is likely to be excited by the first incident  
 408 lobe, and the A0 mode (at  $34.2^\circ$ ) by the second and the third incident lobe.

409 The initial Bertoni and Tamir model plotted in Figure 12.c predicts the re-emission  
 410 of the only mode A1 at  $9^\circ$  (labelled 1) with a slow decrease along the plate because this  
 411 mode is poorly attenuated. However experimentation (Figure 12.b) and modified  
 412 Bertoni and Tamir model (Figure 12.d) reveals strong interferences, proving that other

413 modes are excited by side lobes. The first beam (labelled 1) is the re-emission of the A1  
 414 mode at  $9^\circ$ . The second beam (labelled 2) is directed at  $13.5^\circ$ , which corresponds to the  
 415 interference between A1 and S0 that is excited by the first side lobe: the equation (1)  
 416 evaluates the interference at  $13.6^\circ$ . The third beam is measured at  $18^\circ$  and is the re-  
 417 emission of the S0 mode without interference: the A1 mode has become negligible. The  
 418 last double beam (labelled 4) is measured at about  $25^\circ$ , which is compatible with the  
 419 interference between S0 mode and A0 predicted at  $26.2^\circ$ , the A0 mode being excited by  
 420 the second and third side lobe. Experimentation and our modified Bertoni and Tamir  
 421 model are in good agreement.

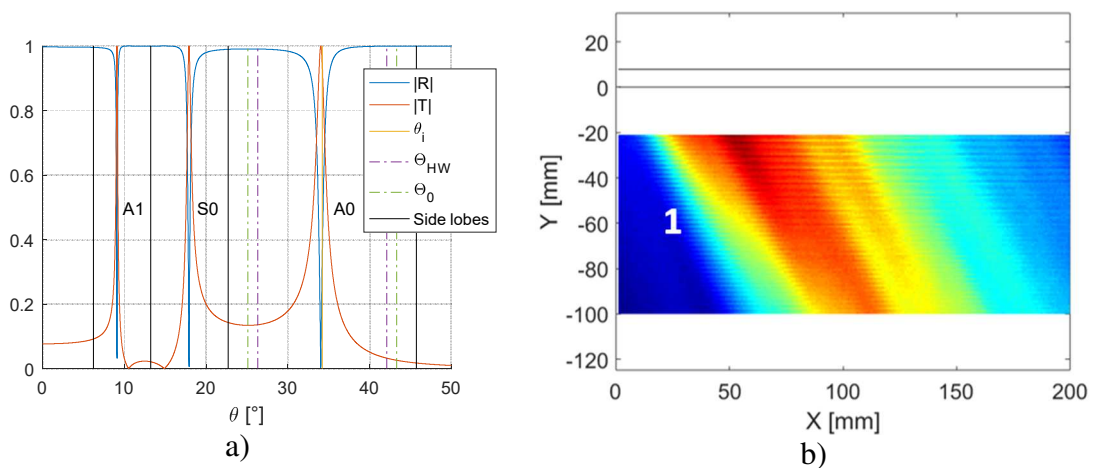
422



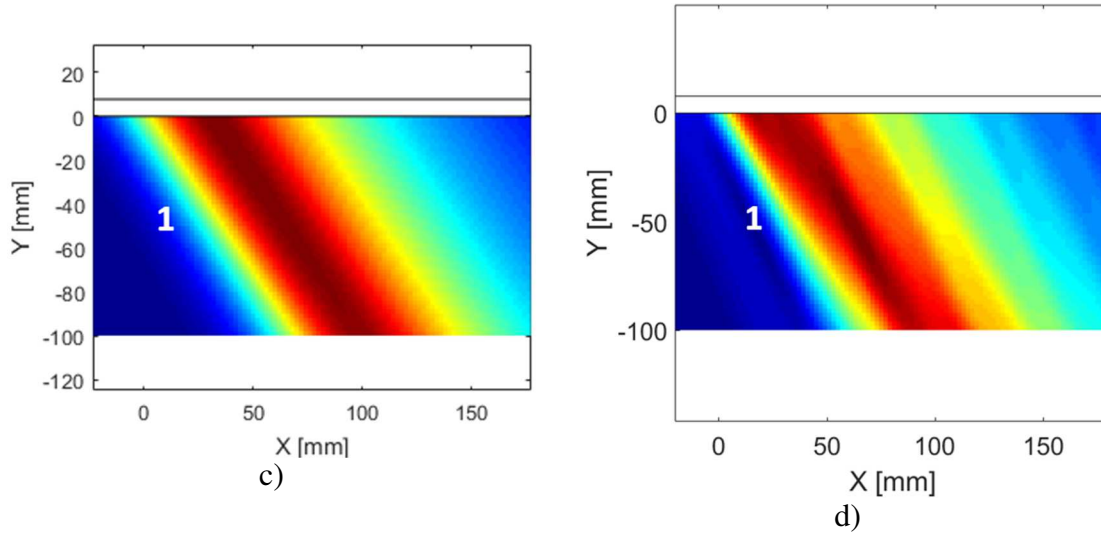
425 Figure 12: a) Reflection and transmission modulus with superposition of the main beam  
 426 spreading angles  $\Theta_{HW}$  and  $\Theta_0$  and incidence angles of side lobes for  $\theta = 9^\circ$  at 250kHz.  
 427 Comparison of the transmitted field: b) experimental C-scan, c) initial Bertoni and Tamir model  
 428 and d) modified Bertoni and Tamir model with side lobes taken into account  
 429

430 Finally, the A0 mode has been targeted at  $= 34.2^\circ$ : this mode has a leaky attenuation  
 431 close to S0 but both are higher than A1. The Figure 13.a shows that the main beam  
 432 excites only the A0 mode, and that S0 and A1 can be excited by the three left side lobes.  
 433 We can expect small interferences with S0 and negligible interferences with A1.

434 The initial Bertoni and Tamir model (Figure 13.c) only predict the re-emission of A0  
 435 (labelled 1) at  $34^\circ$  as expected. This direction was also measured on the experimentation  
 436 (Figure 13.b) and with our modified Bertoni and Tamir model (Figure 13.d). However it  
 437 is difficult to measure other directions Figure 13.b and Figure 13.d because the re-  
 438 emitted field is distorted by interferences of small amplitudes, probably with the S0  
 439 mode.  
 440







441 Figure 13: a) Reflection and transmission modulus with superposition of the main beam  
 442 spreading angles  $\theta_{HW}$  and  $\theta_0$  and incidence angles of side lobes for  $\theta = 34.2^\circ$  at 250 kHz.  
 443 Comparison of the transmitted field: b) experimental C-scan, c) initial Bertoni and Tamir model  
 444 and d) modified Bertoni and Tamir model with side lobes taken into account

445

#### 446 4. CONCLUSION

447 The analytical Bertoni and Tamir model is modified to take into account side lobes  
 448 inherent to an experimental transducer. A finite-element simulation was also ran with  
 449 the same incident bounded beam and validated these two techniques by experimental  
 450 observation. We confirm the importance of taking the side lobes of the incident acoustic  
 451 beam into account, in order to model correctly the re-emitted field that can present  
 452 strong interferences in case of multimodal propagation. These interferences are  
 453 predictable if the incident beam is well known.

454 When Lamb waves are used for NDT, it is usually better to excite a single Lamb  
 455 mode for clarity of signals. Moreover, as a function of the defect, the creation of others  
 456 Lamb modes can occur when the incident Lamb mode is reflecting on the defect. To  
 457 avoid initial multi-modal propagation, one could suppress side lobes by using a

458 nonuniform transducer: such a transducer has his piezo-electric disk dividing into two  
459 zones, enabling a mean windowing of the initial excitation [33,34]. However, we can  
460 reduce the effect of side lobes on the plate by aiming with the main beam the leaky  
461 Lamb mode with the highest leaky attenuation coefficient. Others leaky Lamb modes  
462 are harder to be generated [16] and are likely to be negligible if a side lobe excites them.  
463 However, such highly attenuated modes are bad candidates for long range inspection of  
464 immersed plate. There is a compromise to be found case by case regarding the length of  
465 the plate to be controlled and the purity of the Lamb mode excited.

466 If multiple Lamb modes are generated by the only main beam, we could also increase  
467 its directivity by increasing the transducer diameter. Another way to achieve this goal is  
468 to use higher frequencies (some MHz) with thinner plates (few millimetres) as in [28]:  
469 the main incident beam will have better directivity, and Lamb modes will be easily  
470 decoupled from each other.

471 The finality of this work will be to achieve NDT in several parallel and immersed  
472 plates. To reach this goal, a complete study of leaky Lamb waves that propagates in two  
473 parallel and immersed plate is available in [35], and experimental detection of defects in  
474 the second plate are compared with theory in [36].

475

## 476 **Acknowledgements**

477 This research was supported by the CEA Cadarache centre, France.

478

479 **Appendix: Properties of the plate and water used for numerical applications**

480 The immersed plate is homogeneous, elastic and isotropic in stainless steel (density  
481 of  $7\,950\text{ kg}\cdot\text{m}^{-3}$ , longitudinal and shear velocities respectively of  $5\,750\text{ m}\cdot\text{s}^{-1}$  and  
482  $3\,150\text{ m}\cdot\text{s}^{-1}$ ), with no attenuation due to the material (absorption and scattering). These  
483 values were measured on the stainless steel plate used for experimentation.

484 Water is modelled with a density of  $1\,000\text{ kg}\cdot\text{m}^{-3}$  and a speed of sound equal to  
485  $1\,490\text{ m}\cdot\text{s}^{-1}$ . The viscosity of water is neglected.

486

487 **References**

- 488 [1] F. Jadot, F. Baqué, J.P. Jeannot, G. de Dinechin, J.M. Augem, J. Sibilo, ASTRID  
489 sodium cooled fast reactor: Program for improving in service inspection and  
490 repair, in: 2011 2nd International Conference on Advancements in Nuclear  
491 Instrumentation, Measurement Methods and Their Applications (ANIMMA),  
492 2011: pp. 1–8. doi:10.1109/ANIMMA.2011.6172910.
- 493 [2] F. Baqué, F. Jadot, R. Marlier, J.F. Saillant, V. Delalande, In Service Inspection  
494 and Repair of the sodium cooled ASTRID reactor prototype, in: Proceedings of  
495 ICAPP'15, Nice, France, 2015.
- 496 [3] G. Corneloup, M.-A. Ploix, J.-F. Chaix, I. Lillamand, F. Baqué, Potential of  
497 Ultrasounds for NDT of a structure located behind parallel immersed plates, in:  
498 Review of Progress in Quantitative NonDestructive Evaluation: Volume 30A;  
499 Volume 30B, AIP Publishing, 2011: pp. 1695–1700. doi:10.1063/1.3592132.
- 500 [4] P. Kauffmann, M.-A. Ploix, J.-F. Chaix, C. Gueudré, G. Corneloup, F. Baqué,  
501 Study of Lamb Waves for Non-Destructive Testing Behind Screens, in: 2017 5th  
502 International Conference on Advancements in Nuclear Instrumentation,  
503 Measurement Methods and Their Applications (ANIMMA), EPJ Web of  
504 Conferences, Liège, Belgium, 2018. doi:10.1051/epjconf/201817003005.
- 505 [5] D. Alleyne, P. Cawley, Optimization of lamb wave inspection techniques, NDT &  
506 E International. 25 (1992) 11–22. doi:10.1016/0963-8695(92)90003-Y.
- 507 [6] D. Alleyne, P. Cawley, The Interaction of Lamb Waves with Defects, IEEE Trans.  
508 Ultrason. Ferroelectr. Freq. Control. 39 (1992) 381–397. doi:10.1109/58.143172.
- 509 [7] A.H. Nayfeh, Wave propagation in layered anisotropic media: with applications to  
510 composites, Elsevier, Amsterdam ; New York, 1995.

- 511 [8] P. Wilcox, M. Lowe, P. Cawley, Lamb and SH wave transducer arrays for the  
512 inspection of large areas of thick plates, in: AIP, 2000: pp. 1049–1056.  
513 doi:10.1063/1.1306159.
- 514 [9] M. Castaings, E. Le Clezio, B. Hosten, Modal decomposition method for modeling  
515 the interaction of Lamb waves with cracks, *The Journal of the Acoustical Society*  
516 *of America*. 112 (2002) 2567–2582. doi:10.1121/1.1500756.
- 517 [10] I.A. Viktorov, *Rayleigh and Lamb Waves: Physical Theory and Applications*,  
518 Softcover reprint of the original 1st ed. 1967 edition, Springer, 2013.
- 519 [11] A.H. Nayfeh, P.B. Nagy, Excess attenuation of leaky Lamb waves due to viscous  
520 fluid loading, *The Journal of the Acoustical Society of America*. 101 (1997) 2649–  
521 2658. doi:10.1121/1.418506.
- 522 [12] L.G. Merkulov, Damping of normal modes in a plate immersed in a liquid, *Sov.*  
523 *Phys. Acoust.* 10 (1964) 169–173.
- 524 [13] A.E. Takiy, C. Kitano, R.T. Higuti, S.C.G. Granja, V.T. Prado, L. Elvira, O.  
525 Martinez-Graullera, Ultrasound imaging of immersed plates using high-order  
526 Lamb modes at their low attenuation frequency bands, *Mech. Syst. Signal Proc.* 96  
527 (2017) 321–332. doi:10.1016/j.ymsp.2017.04.021.
- 528 [14] A. Bernard, M.J.S. Lowe, M. Deschamps, Guided waves energy velocity in  
529 absorbing and non-absorbing plates, *J. Acoust. Soc. Am.* 110 (2001) 186–196.  
530 doi:10.1121/1.1375845.
- 531 [15] D.E. Chimenti, S.I. Rokhlin, Relationship between leaky Lamb modes and  
532 reflection coefficient zeroes for a fluid-coupled elastic layer, *The Journal of the*  
533 *Acoustical Society of America*. 88 (1990) 1603–1611. doi:10.1121/1.400319.

- 534 [16] P.D. Wilcox, M.J.S. Lowe, P. Cawley, Mode and transducer selection for long  
535 range lamb wave inspection, *J. Intell. Mater. Syst. Struct.* 12 (2001) 553–565.  
536 doi:10.1106/N9PB-Y62E-P0Y2-50QF.
- 537 [17] A. Pilarski, J.J. Ditri, J.L. Rose, Remarks on symmetric Lamb waves with  
538 dominant longitudinal displacements, *The Journal of the Acoustical Society of*  
539 *America.* 93 (1993) 2228–2230. doi:10.1121/1.406684.
- 540 [18] H.L. Bertoni, T. Tamir, Unified theory of Rayleigh-angle phenomena for acoustic  
541 beams at liquid-solid interfaces, *Applied Physics.* 2 (1973) 157–172.  
542 doi:10.1007/BF00884205.
- 543 [19] P.D. Wilcox, M.J.S. Lowe, P. Cawley, The effect of dispersion on long-range  
544 inspection using ultrasonic guided waves, *NDT & E International.* 34 (2001) 1–9.  
545 doi:10.1016/S0963-8695(00)00024-4.
- 546 [20] Y.-F. Xu, W.-X. Hu, Wideband dispersion removal and mode separation of Lamb  
547 waves based on two-component laser interferometer measurement, *Chin. Phys. B.*  
548 26 (2017) 094301. doi:10.1088/1674-1056/26/9/094301.
- 549 [21] C. Potel, S. Baly, J.F. de Belleval, M. Lowe, P. Gagniol, Deviation of a  
550 monochromatic Lamb wave beam in anisotropic multilayered media: Asymptotic  
551 analysis, numerical and experimental results, *IEEE Trans. Ultrason. Ferroelectr.*  
552 *Freq. Control.* 52 (2005) 987–1001. doi:10.1109/TUFFC.2005.1504021.
- 553 [22] J. Rautenberg, S. Olfert, F. Bause, B. Henning, Validation of analytically modeled  
554 Leaky Lamb radiation using Schlieren photography, in: *Ultrasonics Symposium*  
555 *(IUS), 2012 IEEE International, 2012: pp. 819–822.*  
556 doi:10.1109/ULTSYM.2012.0204.

- 557 [23] N.F. Declercq, J. Degrieck, O. Leroy, Bounded Beam Interaction with Plate-Edge  
558 at Lamb Angle, *Acta Acustica United with Acustica*. 91 (2005) 326–332.
- 559 [24] M. Schmitt, K. Schmidt, S. Olfert, J. Rautenberg, G. Lindner, B. Henning, L.M.  
560 Reindl, Detection of coatings within liquid-filled tubes and containers by mode  
561 conversion of leaky Lamb waves, *Journal of Sensors and Sensor Systems*. 2 (2013)  
562 73–84. doi:10.5194/jsss-2-73-2013.
- 563 [25] T.J. Plona, L.E. Pitts, W.G. Mayer, Ultrasonic bounded beam reflection and  
564 transmission effects at a liquid/solid-plate/liquid interface, *The Journal of the*  
565 *Acoustical Society of America*. 59 (1976) 1324–1328. doi:10.1121/1.381011.
- 566 [26] L.E. Pitts, T.J. Plona, W.G. Mayer, Theory of Nonspecular Reflection. Effects for  
567 an Ultrasonic Beam Incident on a Solid Plate in a Liquid, *IEEE Transactions on*  
568 *Sonics and Ultrasonics*. 24 (1977) 101–108. doi:10.1109/T-SU.1977.30919.
- 569 [27] T.D.K. Ngoc, W.G. Mayer, A General Description of Ultrasonic Nonspecular  
570 Reflection and Transmission Effects for Layered Media, *IEEE Transactions on*  
571 *Sonics and Ultrasonics*. 27 (1980) 229–235. doi:10.1109/T-SU.1980.31182.
- 572 [28] T.D.K. Ngoc, W.G. Mayer, Influence of Plate Mode Structure and Gaussian Beam  
573 Profile Characteristics on Ultrasonic Reflection and Transmission, *IEEE*  
574 *Transactions on Sonics and Ultrasonics*. 29 (1982) 112–114. doi:10.1109/T-  
575 SU.1982.31316.
- 576 [29] M. Aanes, K.D. Lohne, P. Lunde, M. Vestrheim, Beam Diffraction Effects in the  
577 Backward Wave Regions of Viscoelastic Leaky Lamb Modes for Plate  
578 Transmission at Normal Incidence, *IEEE Trans. Ultrason. Ferroelectr. Freq.*  
579 *Control*. 64 (2017) 1558–1572. doi:10.1109/TUFFC.2017.2719627.
- 580 [30] D.T. Blackstock, *Fundamentals of physical acoustics*, Wiley, New York, 2000.

- 581 [31] B. Moudjed, Experimental and theoretical characterization of acoustic streaming.  
582 Prospect of an use for photovoltaic Silicon solidification., Theses, INSA de Lyon,  
583 2013. <https://tel.archives-ouvertes.fr/tel-00958258> (accessed January 3, 2017).
- 584 [32] M. Castaings, C. Bacon, B. Hosten, M.V. Predoi, Finite element predictions for the  
585 dynamic response of thermo-viscoelastic material structures, *J. Acoust. Soc. Am.*  
586 115 (2004) 1125–1133. doi:10.1121/1.1639332.
- 587 [33] D. De Vadder, A. Lhémery, N. Gengembre, A New Ultrasonic Transducer  
588 Combining Three Modes: High Axial Resolution, High Transverse Resolution and  
589 Standard Modes, in: *Review of Progress in Quantitative Nondestructive*  
590 *Evaluation: Volume 15A*, Springer US, Boston, MA, 1996: pp. 979–986.  
591 doi:10.1007/978-1-4613-0383-1\_128.
- 592 [34] A. Lhémery, D. De Vadder, N. Gengembre, Wideband Nonuniformly Excited  
593 Focused Transducers - Theory and Experiments, in: *Review of Progress in*  
594 *Quantitative Nondestructive Evaluation: Volume 15A*, Springer US, Boston, MA,  
595 1996: pp. 963–970. doi:10.1007/978-1-4613-0383-1\_126.
- 596 [35] P. Kauffmann, M.-A. Ploix, J.-F. Chaix, C. Gueudré, G. Corneloup, F. Baqué,  
597 Multi-modal leaky Lamb waves in two parallel and immersed plates: theoretical  
598 considerations, simulations and measurements, *The Journal of The Acoustical*  
599 *Society of America*. 145 (2019) 1018-1030. doi: 10.1121/1.5091689
- 600 [36] P. Kauffmann, M.-A. Ploix, J.-F. Chaix, C. Gueudré, G. Corneloup, F. Baqué,  
601 Non-Destructive Testing of Nuclear Structures behind Screen using Leaky Lamb  
602 Waves, in: *45th Annual Review of Progress in Quantitative Nondestructive*  
603 *Evaluation*, AIP, Conference Proceedings, Burlington, USA, 2018.
- 604



605 **Collected figure captions**

606 Figure 1: Experimental bench: incident bulk waves are sent by a transducer onto a plate  
607 immersed in water (7.8 mm thick and 700 mm long). Leaky Lamb waves are generated  
608 (symbolized by dashed blue arrow), and the transmitted acoustic field (bold red arrows)  
609 is scanned by a needle hydrophone in an area perpendicular to the plate (dash-dotted  
610 yellow line).

611 Figure 2: a) Theoretical reflection and transmission modulus at 500 kHz of the  
612 immersed stainless-steel plate as a function of the incidence angle  $\theta$ . b) Theoretical  
613 leaky attenuation coefficient of Lamb modes for a stainless-steel plate with a thickness  
614 of 7.8 mm.

615 Figure 3: An example of a transmitted beam profile with representation of the main  
616 acoustic beam spreading phenomena

617 Figure 4: a) Reflection and transmission modulus with superposition of the main beam  
618 spreading angles  $\Theta_{HW}$  and  $\Theta_0$  and incidence angles of side lobes for  $\theta = 30.4^\circ$  at  
619 500kHz. Comparison of the transmitted field: b) experimental C-scan, and c) Bertoni  
620 and Tamir model. The plate is illustrated by two parallel black lines and is immersed on  
621 both sides.

622 Figure 5: a) Reflection and transmission modulus with superposition of the main beam  
623 spreading angles  $\Theta_{HW}$  and  $\Theta_0$  and incidence angles of side lobes for  $\theta = 17.2^\circ$  at  
624 500kHz. Comparison of the transmitted field: b) experimental C-scan, and c) Bertoni  
625 and Tamir model, with d) extracted normalised amplitude for  $Y = -20$  mm.

626 Figure 6: Transmitted acoustic field in our configuration computed with the FEM: the  
627 absolute pressure is plotted in water and vertical displacements in the plate

628 Figure 7: Experimental characterisation of the incident acoustic beam used in our  
629 configuration. The red line shows the near field length, representing also the mean  
630 abscissa where the plate is located during experimentation

631 Figure 8: Incident acoustic beam profile with superposition of different model: the  
632 Bertoni and Tamir modelling (Gaussian) and optimised least-squares models (Bessel  
633 Cardinal and Lorentz functions)

634 Figure 9: a) Transmitted acoustic field in our configuration computed with the modified  
635 Bertoni and Tamir model. b) Reflection and transmission modulus with superposition of  
636 the main beam spreading angles  $\Theta_{HW}$  and  $\Theta_0$  and incidence angles of side lobes. c)  
637 Comparison of the amplitude at  $Y = -20$  mm for the experimentation and the Bertoni  
638 and Tamir model with and without side lobes implementation.

639 Figure 10: Comparison of the transmitted field on the same scale: a) experimental C-  
640 scan, b) finite-element simulation and c) modified analytical Bertoni and Tamir model

641 Figure 11: Experimental characterisation of the incident acoustic beam used at 250 kHz.  
642 The red line shows the near field length, representing the mean abscissa where the plate  
643 is located during experimentation

644 Figure 12: a) Reflection and transmission modulus with superposition of the main beam  
645 spreading angles  $\Theta_{HW}$  and  $\Theta_0$  and incidence angles of side lobes for  $\theta = 9^\circ$  at 250kHz.  
646 Comparison of the transmitted field: b) experimental C-scan, c) initial Bertoni and  
647 Tamir model and d) modified Bertoni and Tamir model with side lobes taken into  
648 account

649 Figure 13: a) Reflection and transmission modulus with superposition of the main beam  
650 spreading angles  $\Theta_{HW}$  and  $\Theta_0$  and incidence angles of side lobes for  $\theta = 34.2^\circ$  at 250

651 kHz. Comparison of the transmitted field: b) experimental C-scan, c) initial Bertoni and  
652 Tamir model and d) modified Bertoni and Tamir model with side lobes taken into  
653 account

654

655

656 **Collected table captions**

657 Table 1: Piecewise definition of  $\theta_n$  for  $X$  positive. The definition of  $\theta_n$  for  $X$   
658 negative is based on the same scheme, with directions symmetrical to  $\theta$

659